Available online at www.sciencedirect.com
ScienceDirect
Journal of the European Ceramic Society 31 (2011) 3159–3169
www.elsevier.com/locate/jeurceramsoc

Molecular dynamics simulation on ionic conduction process of oxygen in $Ce_{1-x}M_xO_{2-x/2}$

C.W. Huang [a], W.C.J. Wei [a], C.S. Chen [b,*], J.C. Chen [c]

[a] *Institute of Materials Sci. & Eng., National Taiwan University, Taipei 106, Taiwan*
[b] *Department of Civil Engineering, National Taiwan University, Taipei 106, Taiwan*
[c] *Institute of Atomic and Molecular Sciences, Academia Sinica, Taipei 106, Taiwan*

Available online 15 June 2011

Abstract

Molecular dynamics simulation of CeO_2 doped with M^{3+} (a trivalent cation) with ionic radii ranging from 1.019 Å (Y^{3+}) to 1.160 Å (La^{3+}) were performed to examine the effects of the dopant cation size on ionic conductivity. Interatomic potential parameters were empirically fitted with equilibrium properties and energy barriers from *ab initio* calculations. Vacancy trapping and edge blocking mechanisms were studied. Analysis on vacancy trapping showed that the effect was more pronounced in La- and Y-doped ceria than those doped with Gd and Sm. Analysis of the edge blocking effect showed that larger-sized dopants would limit the available pathways for vacancy hopping. The combined effects satisfactorily explained the influence of the dopant cation size on the ionic conductivity of heavily doped ceria.

Keywords: Ceria; Dopant; Ionic conduction; Molecular dynamics; Vacancy trapping

1. Introduction

Ceria (CeO_2) has drawn much attention lately as it has become a promising choice for an electrolyte in intermediate-temperature solid oxide fuel cell (IT-SOFC).[1–5] For fuel cell applications, ceria is often doped with accepter oxides to enhance its ionic conductivity. In general, the ionic radius of dopant cation is considered to be a critical factor for the selective dopant in ceria and related fluorite oxides.[2] For traditional M^{3+} (trivalent cation) doped CeO_2, the ionic conductivity increases with an increase of the radius of the trivalent dopant ion, $r(M^{3+})$ until the radius reaches its maximum value, M = Gd or Sm. After a crossover of the size occurs, the ionic conductivity decreases.[2,3] Thus, it is very important to understand the underlying mechanisms of the $r(M^{3+})$ dependency; such understanding will help us design novel multiple-doping ceria or similar ionic conductive systems in the future.

The dependency of ionic conductivity on a dopant cation can be reasoned from various perspectives. In some earlier studies, the ionic conductivity was simply attributed to the change of lattice constant after doping.[3,4] For larger-sized dopant cations, the lattice of ceria tends to expand, whereas for smaller-sized dopants, the lattice tends to contract. Gd_2O_3 and Sm_2O_3 were rationalized as the optimized oxides since they led to a minimum change of the lattice constant. Recent atomistic simulation studies have provided a more detailed understanding based on atomic-scale defect chemistry.[5] Two different mechanisms for dopant-size dependency have been suggested. The first is related to the difference in the association effect between the counter-charged oxygen vacancy ($V_O^{\bullet\bullet}$) and the substituted trivalent dopant (M'_{Ce}). Several atomistic calculations suggested that the association energy of the associated defects, $\{M_{Ce}V_O\}^{\bullet}$ and $\{2M_{Ce}V_O\}$, reached a minimum value when M is Gd.[6–9] The second mechanism is related to the edge blocking effect revealed from detailed *ab initio* calculations.[9–11] It suggests that the hindrance of oxygen hopping occurs when large-size solute ion is present at the midway of the hopping path. From the viewpoint of edge blocking, a large M'_{Ce} should not be favorable for oxygen diffusion.

Most of the aforementioned atomistic simulations were performed based on energy minimization techniques (0 K). The calculated results are usually based on a minimum number of defects, i.e., generally within a dilute dopant concentration. It is conceivable that in such dilute concentration of defects, the influence of defect association should overwhelm that of edge blocking due to its long-range electrostatic nature.

* Corresponding author.
E-mail address: dchen@ntu.edu.tw (C.S. Chen).

0955-2219/$ – see front matter © 2011 Elsevier Ltd. All rights reserved.
doi:10.1016/j.jeurceramsoc.2011.05.029

However, doped ceria in a concentrated range (for example, $Ce_{1-x}M_xO_{2-x/2}$ at $x > 0.08$) is much closer to practical usages.[12] It had been reported that the edge blocking alone can significantly affect the composition–conductivity relationship in similar zirconia-based systems.[13–15] Consequently, in order to correctly model the ion conduction in heavily doped ceria, a simulation scheme taking both mechanisms into consideration is required. To date, the ion conduction behavior in heavily doped ceria has not been studied in detailed atomistic simulations.

Generally speaking, molecular dynamics (MD) simulation is a preferred tool for simulating atomic diffusion and conduction process. In MD simulations, motions of ions are actually resolved, and direct calculation of atomic diffusivity from atomic trajectory can be performed. Therefore, MD simulation bears a closer resemblance to experimental conditions, and can be properly used to study ionic conduction in various compositions. Although several MD simulation studies of doped ceria are available,[16–18] comparative studies of the effect of different dopant types using MD simulation are rare. In fact, the only relevant work to our knowledge is the study by Hayashi et al.[17] on Y-, Gd- and La-doped ceria. From their results, Gd-doped ceria exhibited the highest oxygen diffusivity, in agreement with experimental observations. However, the underlying mechanisms relating to ionic size dependency were not analyzed in depth.

In this study, we examine the effect of dopant cation radius on ionic conduction process and analyze the underlying mechanisms using MD simulations. Four trivalent dopants (Y, Gd, Sm, and La) with ionic radii ranging from 1.019 Å (Y^{3+}) to 1.160 Å (La^{3+}) are investigated. The dopant level corresponding to maximum conductivity and activation enthalpies are analyzed. The ionic conductivities at a wide composition range (within concentrated dopant level) and their temperature dependency are presented.

2. Methodology

2.1. Parameterization of interatomic potentials

The crystal structure of CeO_2 is fluorite, with the space group Fm3m. Fig. 1(a) shows the unit cell of CeO_2, which consists of four Ce atoms residing at the 4a sites and eight O atoms at the 8c sites. The interatomic potentials adapted were electrostatic in combination with a Buckingham type short-range potential. The potential parameters for Ce^{4+}–O^{2-} and O^{2-}–O^{2-} pairs were taken from Inaba et al.[18] For the M^{3+}–O^{2-} potentials, we adjusted the parameters suggested by Hayashi et al.[17] in order to correlate with measured lattice constants of $Ce_{1-x}M_xO_{2-x/2}$ and energy barriers from *ab initio* calculations. A few candidates of the M–O potential parameters could be found to predict the measured lattice constants. We then used energy barriers from *ab initio* calculations (described below) as the benchmark to find the desirable set of the M–O potential parameters. The energy barriers for oxygen hopping under specific atomic configurations are adopted; these configurations are illustrated in Fig. 1(b).

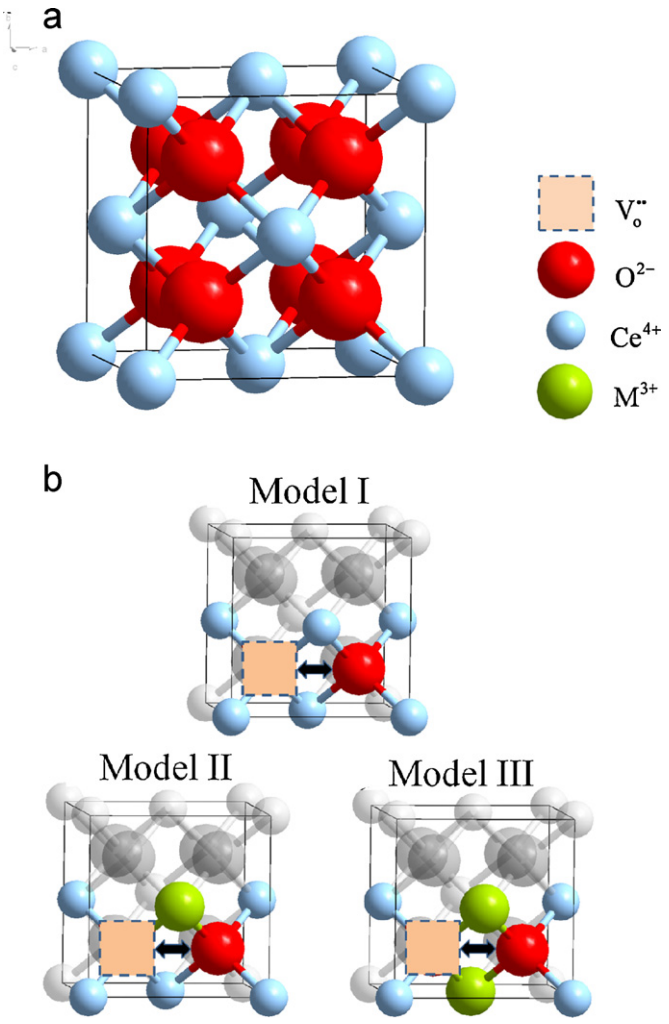

Fig. 1. (a) The crystal structure of a CeO_2 unit cell. (b) Illustration of oxygen hopping into an adjacent vacant site in the CeO_2 lattice. Models I, II and III represent different local structures for oxygen hopping. It should be noted that, the unit cell shown here is only for illustration. For NEB calculation we used a $2 \times 2 \times 3$ supercell.

The new potential parameters are listed in Table 1. Calculated lattice constants from these parameters gave excellent agreement with the experimental measurements[19] (Fig. 2). Table 2 shows the comparison of the calculated energy barriers from the literature,[10] independent *ab initio* calculations performed herein and MD with the new potential parameters. Again, calculated energy barriers from these parameters gave excellent agreement with those from *ab initio* calculations. Finally, we remark that although the new potential parameters perform very well for a $Ce_{1-x}M_xO_{2-x/2}$ system, they do not perform equally well for the bulk M_2O_3 phase.

2.2. Molecular dynamics simulation

To perform MD simulation, a supercell consisting of $5 \times 5 \times 5$ unit cells of pure CeO_2, with total 500 Ce and 1000 O atoms, was used as the initial model. The $Ce_{1-x}M_xO_{2-x/2}$ was then generated by replacing the $500x$ of Ce^{4+} with M^{3+} and by removing $250x$ of oxygen atoms as vacancies. For

Table 1
Potential parameters used in the present study.

Electrostatic potential $E(r) = -\frac{q_i q_j}{4\pi\varepsilon_0 r}$	
Species	Charge (elementary charge)
O	−1.35
Ce	2.7
Y, La, Sm, Gd	2.025

Short-range potential with Buckingham's form: $S(r) = A \exp\left(\frac{-r}{\rho}\right) - \frac{C}{r^6}$

Pair	A (eV)	ρ (Å)	C (eV Å^6)
Ce–O	30887.45	0.2114	0.00
O–O	980.06	0.332	17.384
La–O	1442.0	0.3144	0.00
Sm–O	1578.0	0.2953	0.00
Gd–O	1385.0	0.298	0.00
Y–O	2500.0	0.2685	0.00

Note: The Ce^{4+}–O^{2-} and O^{2-}–O^{2-} short-range potential parameters were taken from Hayashi et al.[17] The parameters originally appeared in Busing approximation of Born–Mayer–Huggins form and have been converted to the Buckingham's form herein.

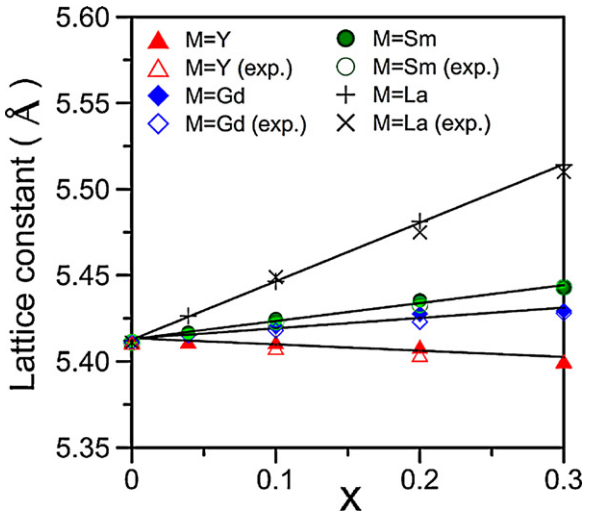

Fig. 2. Lattice constants of $Ce_{1-x}M_xO_{2-x/2}$ (298 K, 1 ns) from calculations and from experimental measurements.[19].

Table 2
Calculated energy barriers for oxygen hopping, with the reported simulation result.

	ab initio	Nakayama and Martin[10]	Present MD simulation
Model I (eV)			
	0.488	~0.482	0.480
Model II (eV)			
M = Y	0.523	~0.533	0.519
M = Gd	0.570		0.564
M = Sm	0.637		0.631
M = La	0.827		0.819

Note: Models I and II refer to the hopping under different atomic configurations, as illustrated in Fig. 1.

Table 3
The effect of cell size on calculated oxygen diffusivity of $Ce_{0.8}Gd_{0.2}O_{1.9}$ at 1273 K for 2 ns.

Cell size	# of atoms	Oxygen diffusivity (m^2/s)	Stdev
5 × 5 × 5	1500	2.45×10^{-11}	1.19×10^{-12}
6 × 6 × 6	2592	2.33×10^{-11}	5.24×10^{-13}
7 × 7 × 7	4116	2.38×10^{-11}	5.20×10^{-13}
8 × 8 × 8	6144	2.46×10^{-11}	1.99×10^{-13}

Note: for each cell size, five simulations with different randomly assigned initial configurations of M'_{Ce} and $V_O^{\bullet\bullet}$ were performed. The oxygen diffusivity is the average and stdev is the standard deviation.

a heavily doped ceria structure, the geometric distribution of dopant cations used in Hayashi et al.[17] and Inaba et al.[18] was adapted in which a random distribution of M^{3+}–M^{3+} pairs was assumed. In this study, five random models with different distributions of dopant cations and oxygen vacancies were generated for all compositions. Finite size effect was investigated by systematically increasing the size of the simulation box. Table 3 lists the calculated oxygen diffusivity for different cell sizes. It appeared that the predicted value of oxygen diffusivity was not sensitive to the cell size.

In order to obtain adequate time sampling, the simulation time was prolonged to 5 ns, within which 1 ns is for equilibrium run and 4 ns is for production run and data collection. During the simulation, the Hamiltonian converged quickly (~50 ps) and did not fluctuate dramatically for the rest of simulation time. All MD calculations were performed using the DL_POLY code[20] under the N–P–T (constant particle number, hydrostatic pressure and temperature) ensemble. The time-step was 2 fs (2×10^{-15} s), and the Nosé–Hoover algorithm with 0.5 ps thermostat relaxation time and 0.8 ps barostat relaxation time was used to effectively control the temperature and pressure.[21,22] An Ewald Sum was applied to calculate the electrostatic energy with a 1.3 nm real-space cut off.

2.3. *Ab initio* calculation of the energy barrier

The Vienna *ab initio* simulation package (VASP)[23,24] was used to find the energy barriers of the atomic configurations depicted in Fig. 1(b). VASP provides fast and efficient algorithms to find the electronic ground state of the system. The generalized-gradient approximation suggested by Perdew et al.[25] was applied to calculate the exchange correlation energy. The effects of core electrons were treated by the projector-augmented wave method.[26,27] A supercell consisting of 2 × 2 × 3 unit cells of CeO_2 was built at first. Single oxygen was then removed to form a single - $V_O^{\bullet\bullet}$ system; this was followed by substituting 0/1/2 neighboring cerium with trivalent dopant to conform to the models for oxygen hopping (Model I/II/III as shown in Fig. 1(b)). The 3 × 3 × 2 Monkhorst-Pack k point mesh[28] and a 400 eV cut-off energy for plane wave were used for *ab initio* calculations. For all trivalent lanthanide elements, localized 4f electrons were treated as part of inner-shell electrons, which is a conventional scheme for compounds with fully ionized lanthanide

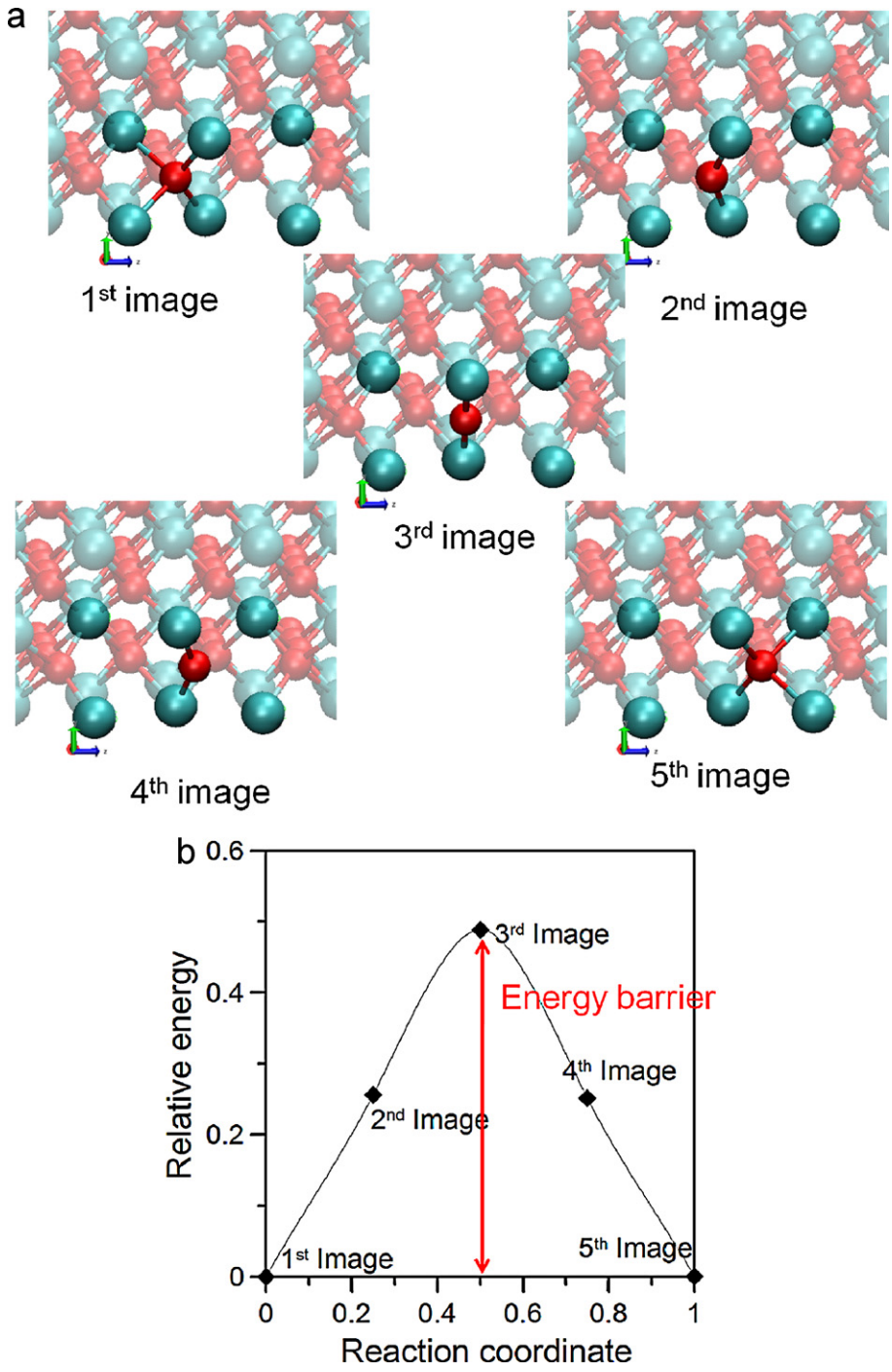

Fig. 3. (a) Illustration of the five images used for NEB calculations. (b) The obtained energy profile of the 5-image NEB calculations.

elements and favors the convergence of electronic configuration calculations. All the *ab initio* calculations were performed under the constant volume constraint. The cell parameters were determined from an independent calculation of a defect-free $2 \times 2 \times 3$ supercell, for which cell and atoms were relaxed simultaneously.

Energy barriers of the hopping process based on *ab initio* calculations were evaluated by the nudged elastic bands (NEB) method.[29] The NEB was performed with five images as depicted in Fig. 3(a), in which Model I was used for illustration and only a fraction of the supercell was shown. It should be noted that the first and the fifth images are the initial and final states, which were fully relaxed prior to the NEB calculations. In order to locate the saddle point, the climbing image modification of the NEB method[30] was adopted. Fig. 3(b) shows the obtained energy profile, in which the energy barrier was defined as the energy difference between the third image (for which the oxygen actually located at the midpoint of hopping), and the initial image. We finally remark that the energy barrier for MD was determined from potential energy

surface by moving an adjacent oxygen atom into a vacant site. The operation and calculations were supported by the GULP code.[31]

3. Results and discussion

3.1. Oxygen diffusivity and ionic conductivity

The ionic conductivity (σ) was evaluated from the self diffusivity of oxygen ions, described by the Nernst–Einstein (N–E) relation:

$$\sigma = \frac{nq^2 D}{kT}, \quad (1)$$

where n is the concentration of a mobile charged species, q is the charge it carries, and D refers to its self diffusivity. It is worth noting that the N–E relation is strictly valid only in a dilute defect concentration. Our evaluation of conductivity is based on the assumption that the conductivity correlation effect can be ignored. The approximation is valid as our system exists in the absence of external fields and thus should not be far from the equilibrium state.[32] In the MD simulation, D of any species can be related with its motion *via* Einstein's equation:

$$\frac{1}{N}\sum_{i=1}^{N}[r_i(t) - r_i(0)]^2 = 6Dt. \quad (2)$$

The left-hand side is also known as the mean-square displacement (MSD), where r_i represents the position of an atom i, and N corresponds to the total number of the species of interest.

Eq. (2) shows that atomic diffusivity is associated with the slope of MSD–time plot. Care must be taken that an essential linearity of MSD–time is required for reasonable evaluation of the diffusivity. For example, the MSD–time plots of Gd- and Y-doped CeO_2 are shown in Fig. 4. The straight lines were linearly fitted, corresponding to the data points beyond 1000 ps (1 ns). It was found that the coefficient of determination R^2 values were larger than 0.95 for all compositions. Thus, the diffusivities at $T \geq 1073$ K could be accurately calculated from the data beyond 1 ns.

Fig. 5(a) plots the calculated ionic conductivity versus $r(M^{3+})$ and the experimental results reported in the literature. In our calculations, Gd–CeO_2 exhibited the highest conductivity. Some discrepancies are noted between different sets of experiments: among the four types of dopants, Sm–CeO_2 exhibited the highest conductivity in the studies by Eguchi et al.[33] and Balazs and Glass,[34] whereas Gd–CeO_2 exhibited the highest conductivity in Vanherle et al.[35] The discrepancies between the measured values indicated the possible interference of microstructures.[36] The conductivity of La-doped CeO_2 reported by Balazs and Glass[34] was apparently lower than that measured by Eguchi et al.[33] The reason for such disagreement was because the La–CeO_2 sample prepared by Balazs and Glass[34] was not fully densified and less homogeneous in phase content. Consequently, the La-doped CeO_2 conductivity value reported by Balazs and Glass[34] should be discarded.

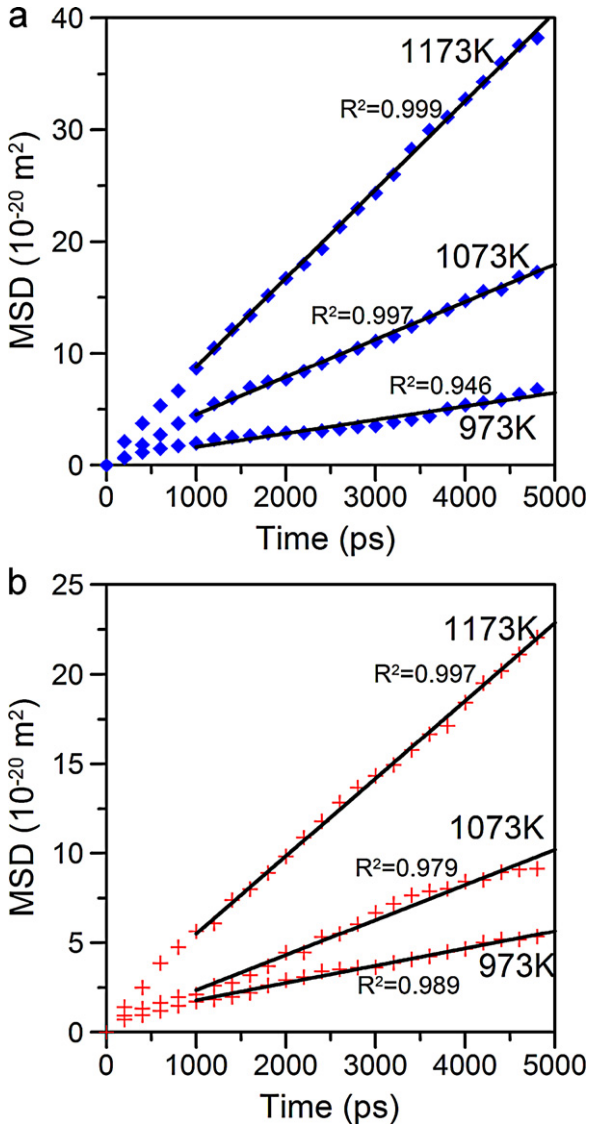

Fig. 4. MSD–time plot of (a) $Ce_{0.8}Gd_{0.2}O_{1.9}$ and (b) $Ce_{0.8}Y_{0.2}O_{1.9}$. The linear fitting corresponds to the data points between 1000 and 5000 ps. The coefficient of determination R^2 values of the fittings are also shown in the figure.

With the above assessment, we observed that the simulated values agreed very well with experimental measurements qualitatively but were consistently lower than the measured values. This was counter-intuitive since the existence of grain boundary and impurity in the experimental samples should be detrimental to the ionic conductivity and the values obtained from theoretical calculations should be higher than the measured ones. The reason for the contrary results is yet to be clarified. One possibility is that the proposed interatomic potential may not be good enough to give a precise prediction on the interaction between vacancy and trivalent cation which will affect the calculated ionic conductivity. To quantify such effect requires the binding energy of V_O–M_{Ce} pair, but such calculations are currently difficult to be obtained directly from *ab initio* simulations. These calculations will be a subject of future studies.

The variation of ionic conductivity with composition was also analyzed. In Fig. 5(b), the x value associated with the highest

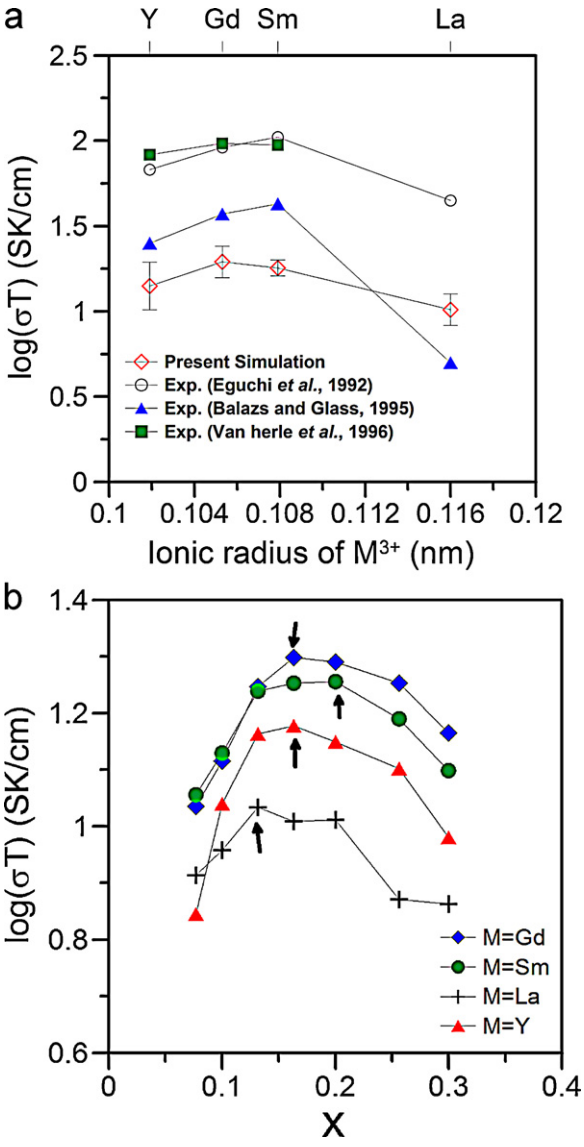

Fig. 5. Simulated ionic conductivity at 1073 K vs (a) $r(M^{3+})$ in $Ce_{0.8}M_{0.2}O_{1.9}$ with experimental data[26–28] (b) composition (x) in $Ce_{1-x}M_xO_{2-x/2}$ (the arrows indicate the composition associated with x_M).

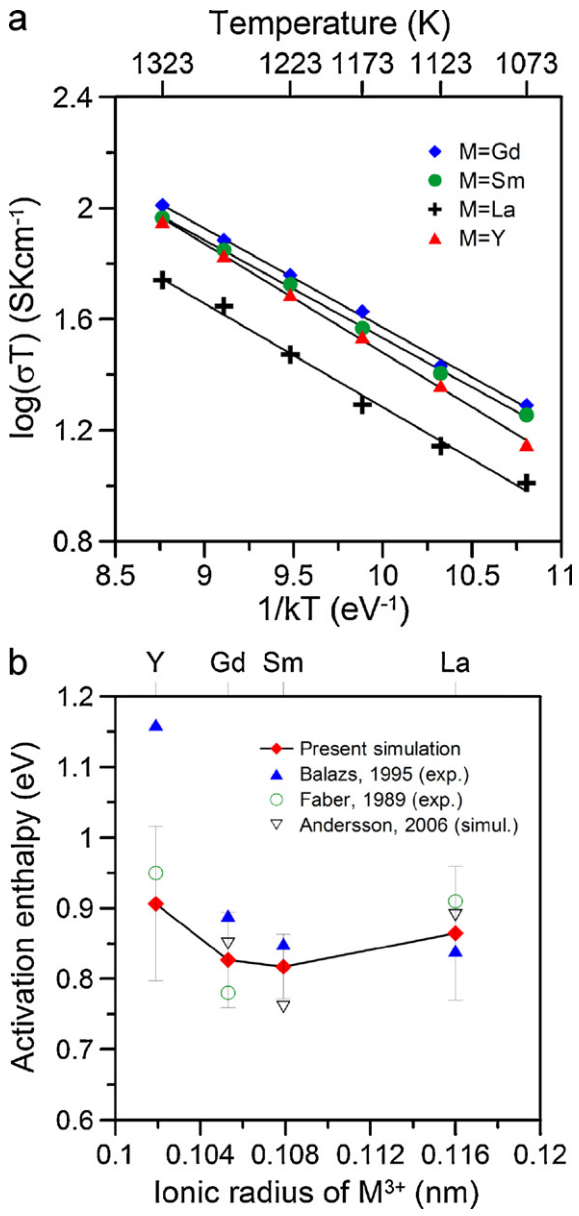

Fig. 6. (a) Arrhenius plots of simulated ionic conductivities of $Ce_{0.8}M_{0.2}O_{1.9}$. (b) Calculated activation enthalpies vs $r(M^{3+})$ in comparison with experimental results and the *ab initio* simulation results reported by Andersson et al.[9].

ionic conductivity in $Ce_{1-x}M_xO_{2-x/2}$ is marked and denoted as x_M. We observed that the predicted x_M ranged between 0.16 and 0.20 for Gd-, Sm- and Y-doped CeO_2, and was around 0.13 for La-doped CeO_2. For M = Gd, Zhang et al.[37] suggested an x_M of 0.20, and Guan et al.[38] reported a value of 0.15, while Steele[39] argued that x_M should occur at 0.1. Zhan et al.[40] measured a x_M value of 0.2 for M = Sm. Values of 0.16–0.2 for M = Y and La have also been reported.[34,41,42] The best dopant values x_M for four elements predicted from the simulations ranged from 0.1 to 0.2, which were consistent with the experimental findings.

The temperature dependency of ionic conductivity is depicted in Fig. 6(a) using an Arrhenius plot. The $\ln(\sigma T) - 1/kT$ plots are essentially linear, as an indication that only one mechanism dominates the ionic conduction for all doped ceria in this temperature range. Consequently, the slope, i.e., the activation enthalpy required for conduction under this mechanism, was calculated. The activation enthalpies versus $r(M^{3+})$ of $Ce_{0.8}M_{0.2}O_{1.9}$ calculated at 1073–1323 K in comparison with experimental results are shown in Fig. 6(b). Although considerable variations exist in our simulation results, the trend is in general agreement with experimental results. The *ab initio* simulation predicted a minimized activation enthalpy[9] for the dopant with an atomic number between Pm and Sm ($61 \leq z \leq 62$), which is also consistent with our MD prediction.

3.2. Vacancy trapping effect

The defect association mechanism accounting for the relationship between σ and $r(M^{3+})$ was investigated. The association can be thought of as oxygen vacancies being trapped in the neighboring sites of M'_{Ce}. The diffusivity of cations in fluorite oxides is about 9–10 orders lower than that of oxygen.[43] Since cations

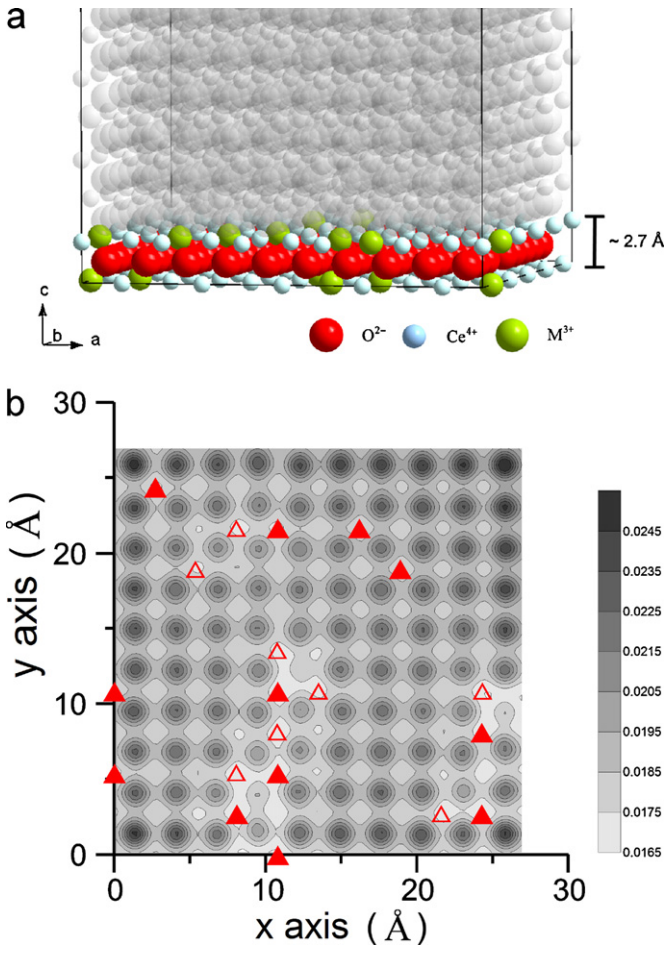

Fig. 7. Illustration of (a) a slice of the simulation cell (blue, red and green spheres represent the Ce^{4+}, O^{2-} and M^{3+} atoms, respectively) used for the subsequent analysis of oxygen density distribution and (b) contour plot of time–averaged oxygen distribution in the slice (the cell corresponds to $Ce_{0.8}Y_{0.2}O_{1.9}$ at 1073 K and data were collected during a 5 ns simulation run). The closed and open triangles represent the M^{3+} at the top and bottom cation planes, respectively. Note that the view is along the *c*-axis. (For interpretation of the references to color in this figure legend, the reader is referred to the web version of the article.)

are virtually immobile, vacancy trapping results in a decrease in oxygen mobility.

The vacancy-trapping phenomenon can be visualized by analyzing the time–averaged distribution of oxygen ions at the selected sites in the simulation cell. Fig. 7(a) shows a slice of a simulation cell (colored part) used for the subsequent analysis of the oxygen density distribution. The atom positions were analyzed per 1000 time steps (2 ps). The oxygen density in a volume was defined by dividing the number of oxygen atoms at a particular site by the total number of records. The contour plot of the oxygen density distribution projected on the slice is shown in Fig. 7(b). The darker points in the figure indicate the regular oxygen sites in a CeO_2 lattice. We observed that several anion sites exhibited lower oxygen densities. The oxygen sites surrounded by triple Y ions tended to be less occupied (e.g. the oxygen sites with coordinates about (9.5,4.7) and (12,12)). This implies that possible vacancy-trapping sites occur close to the Y_{Ce} clusters. This vacancy-trapping phenomenon is independent of the initial configuration of cation impurities. Finally, the

Table 4
Linear regression result based on the model of $Ce_{0.8}M_{0.2}O_{1.9}$. The errors were given as ±1 standard deviation, which is calculated from the results of 5 simulation cells with different intial vacancies and M^{3+} distributions.

Doped element	$r(M^{3+})$ (Å)	β_1	β_2
Y	1.019	-0.07562 ± 0.00143	-0.00044 ± 0.00084
Gd	1.053	-0.05518 ± 0.00123	-0.01326 ± 0.00072
Sm	1.079	-0.03116 ± 0.00140	-0.01873 ± 0.00082
La	1.160	$-6.0 \times 10^{-5} \pm 0.00185$	-0.04150 ± 0.00109

oxygen distribution of the Gd, Sm and La doped ceria systems with an identical spatial distribution of M^{3+} was investigated, and shown in the Fig. 8. The geometric relationship between oxygen density and M^{3+} ions differs for differently doped ceria.

Two types of $\{M_{Ce}V_O\}^\bullet$ associative defects, the first-neighbor and second-neighbor associations, have been widely discussed in the literature.[5] In heavily doped ceria, a high fraction of the oxygen sites are surrounded by trivalent cations at first and/or second-neighbor distances. In order to identify the type of vacancy-trapping mechanism in differently doped ceria, the geometric relationship between oxygen occupancy and number of M^{3+} within the first- or second- neighbor shell was investigated in the following.

The numbers of M^{3+} at the first- and second-neighbor shell around a given oxygen site were identified and denoted as n_i^f and n_i^s. We subsequently performed a two-variable linear regression analysis to find the correlation of the oxygen density at site i (O_i) to n_i^f or n_i^s. The regression was based on a statistical model, which showed the oxygen occupancy (O_i) as a function of n_i^f and n_i^s:

$$O_i = \beta_0 + \beta_1 n_i^f + \beta_2 n_i^s + \varepsilon_i, \quad (3)$$

where the oxygen occupancy (O_i) was calculated by integrating the oxygen density over the volume of the oxygen site.[44] β_0, β_1 and β_2 were the coefficients of the regression model and ε_i represented a random variable following a normal distribution with a zero mean. If β_1 and β_2 were negative, this implied that the formation of oxygen vacancies was likely located in the neighborhood of M'_{Ce} sites. The results of regression are listed in Table 4. All of the β_1 and β_2 values were negative, implying that the vacant site i was surrounded by trivalent cations. Meanwhile, β_1 became more negative as $r(M^{3+})$ decreased, while for M = La, β_1 was obtained with little relevancy. These results indicated that oxygen vacancies for smaller-sized M-doped ceria preferred to occur at the sites with a greater n_i^f. For β_2, a reversed trend was found: β_2 was more negative and significant as $r(M^{3+})$ increased. We thus conclude that for M = Y, Gd and Sm, first-neighbor trapping of $V_O^\bullet$ by M'_{Ce} is preferred, while for M = La, second-neighbor trapping is preferred.

Kilner[5] has recently reviewed the first-/second-neighbor favored vacancy-trapping for differently doped ceria. In a static lattice simulation by Minervini et al.,[7] it was suggested that for the defect $\{M_{Ce}V_O\}^\bullet$, the second-neighbor binding energies for M = La was higher than the first-neighbor binding energies. However, for M = Y and Gd, the first-neighbor binding was more

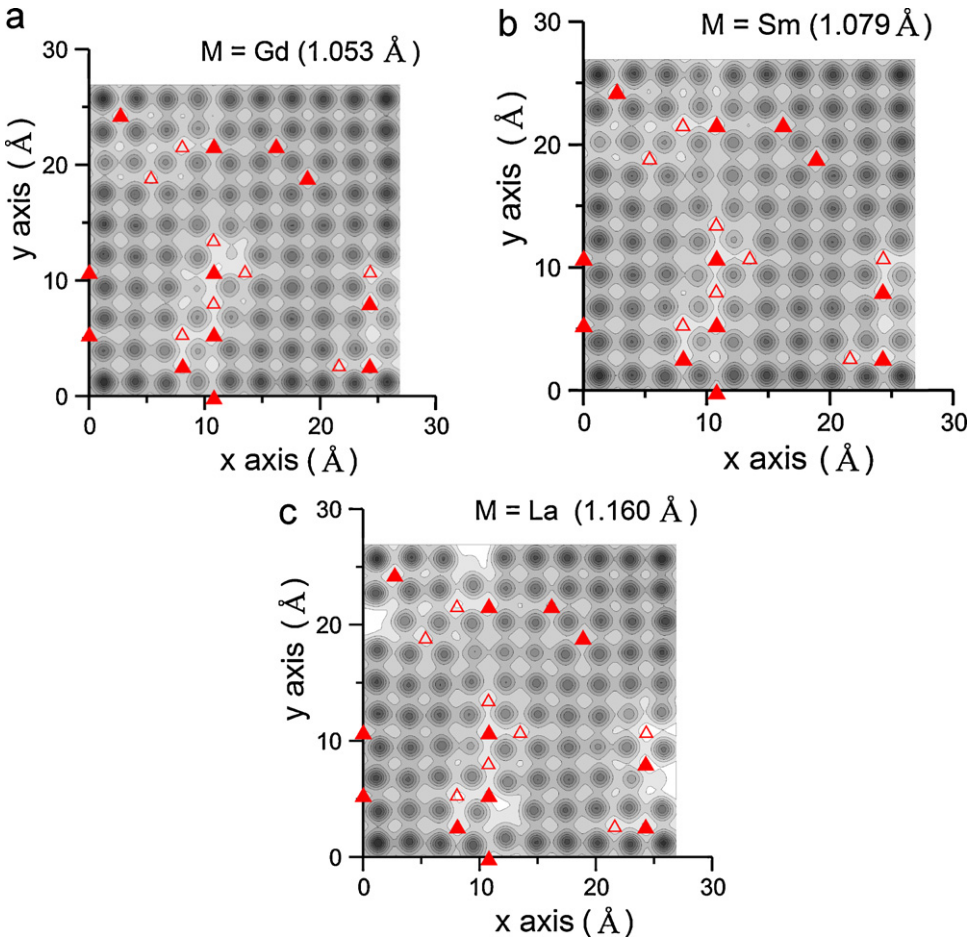

Fig. 8. Time-averaged oxygen density in a slice of (a) $Ce_{0.8}Gd_{0.2}O_{1.9}$ and (b) $Ce_{0.8}Sm_{0.2}O_{1.9}$ (c) $Ce_{0.8}La_{0.2}O_{1.9}$ $5 \times 5 \times 5$ cell at 1073 K.

energetically preferred. Similar results were also reported by Andersson et al.[9] using *ab initio* studies on lanthanum series ions. MD simulation results by Hayashi et al.[17] and Cheng et al.[16] and a calorimetric study by Navrotsky et al.[45] also suggested that for M = Y and Gd, first-neighbor trapping was preferred. It is interesting to note that our results on second-neighbor favored vacancy-trapping for La agree with those from Minervini et al.[7] and Anderson et al.[9] These findings contradict with those from Hayashi et al.[17] and Navrotsky et al.[45] where the oxygen vacancies were found to favor the sites locating at the first-neighbor in La-doped ceria. As our findings agree with those from *ab initio* simulations by Andersson et al.,[9] this also gives evidence that the potential derived in this study is superior to that from Hayashi et al.[17]

The result of the Table 4 also suggests the existence of [multiple M'_{Ce}–single $V_O^{\bullet}$] defect clusters. Indeed, we found that an oxygen site surrounded by more dopants at either first neighbor or second neighbor tended to be more vacant. For example, in Y-doped CeO_2, a site surrounded by four first-neighbor Y was found to have an average occupancy of only 0.02. This should give evidence for the presence of a $[4Y_{Ce} - V_O]''$ defect complex. Furthermore, a site with seven second-neighbor La was also found to exhibit only 0.006 average occupancy; this can also be regarded as formation of a $[7La_{Ce} - V_O]^{5-}$ complex.

In addition to the geometries of vacancy trapping, it is also important to quantify the effect on ionic diffusion process. In order to quantify vacancy trapping, an analysis of the distribution of O_i was performed. This was achieved by collecting the data value of O_i of all oxygen sites. For the ensemble with a constant number of particles, the integration over all the oxygen sites should be a constant for a given composition, i.e.,

$$\frac{\sum_i^N (1 - O_i)}{N} = [V_O^{\bullet}]^S, \tag{4}$$

where N is the total number of oxygen sites in our simulation cell and $[V_O^{\bullet}]^S$ is the averaged site fraction of oxygen vacancy. In $Ce_{1-x}M_xO_{2-x/2}$, $[V_O^{\bullet}]^S$ is related to the composition (x) as:

$$[V_O^{\bullet}]^S = 1 - \left(1 - \frac{x}{4}\right) = \frac{x}{4}. \tag{5}$$

Thus, $[V_O^{\bullet}]^S$ is 0.05 for $Ce_{0.8}M_{0.2}O_{1.9}$. By defining a threshold value of occupancy, O_t, as a criterion for a "deep-trapping site",

Table 5
Calculated $d(O_t)$ and percentage of strong vacancy-trapping sites (sites with $O_i < O_t$) of $Ce_{0.8}M_{0.2}O_{1.9}$ at 1073 K. The errors were given as ±1 standard deviation, which is calculated from the results of 5 simulation cells with different intial vacancies and M^{3+} distributions.

Dopant (M)	$d(O_t)$ (%)	Percentage of strong vacancy-trapping sites (%)
Y	21.82 ± 8.06	2.22 ± 1.51
Gd	9.98 ± 4.00	0.78 ± 0.36
Sm	9.90 ± 4.90	0.78 ± 0.37
La	33.60 ± 8.46	2.36 ± 0.55

the percentage of deep-trapped vacancy can be quantified as a function $d(O_t)$:

$$d(O_t) = \frac{\sum_{O_i<O_t}(1-O_i)}{\sum_{i}^{N} 1-O_i} \times 100\% = \frac{\sum_{O_i<O_t}(1-O_i)}{N[V_O^{\bullet}]^S} \times 100\% \quad (6)$$

In this study, O_t for a composition with $x = 0.2$ was chosen as 0.5, since this value was significantly lower than the average occupancy, 0.95. The calculated d values are listed in Table 5. Taking M = Y as an example, 1.68% of strong vacancy trapping sites existed in the lattice, these sites actually trapped 21.8% of total oxygen vacancies. In comparison, the $d(O_t)$ for Gd/Sm-doped ceria was significantly lower than that of the M = Y/La cases. This indicates that the vacancy-trapping effect is more pronounced in Y/La-doped ceria than that in Gd/Sm-doped ceria.

Based on the aforementioned analyses, oxygen vacancies tend to be trapped at the first-neighbor of M'_{Ce} in Y-, Gd- and Sm- doped ceria, while for M = La, second-neighbor trapping is preferred. In addition, the vacancy-trapping is more prevalent in higher $d(O_t)$ and leads to the negative correlation between $d(O_t)$ and conductivity. In other words, the ionic conductivity in lower $d(O_t)$ (M = Sm/Gd) is higher than those in higher $d(O_t)$ (M = La/Y). We performed a few analyses with varying O_t (0.5–0.8) and found that the order of $d(O_t)$ (La > Y > Sm ≒ Gd) was insensitive to the choice of O_t. As it is not possible to differentiate the order of $d(O_t)$ for Sm– and Gd–CeO_2, this suggests that the vacancy trapping effect alone is not sufficient to explain the highest conductivity of Gd–CeO_2.

3.3. Edge blocking effect

The term "edge blocking" refers to oxygen hopping (or oxygen-vacancy exchange) hindrance when a larger dopant cation resides in the hopping path. As illustrated in Fig. 1(b), an oxygen ion passes through the sharing edge of two tetrahedra and preferentially hops to the nearby vacant site. In several *ab initio* studies on zirconia and ceria systems,[9,14,46] the energy barrier for the hopping is found to increase when one (or both) of the host cations on the edge is substituted by larger trivalent cation(s). The same trend was observed in this study (Table 2). The energy barriers of hopping based on model II increased with an increase of $r(M^{3+})$. Similar trends were found for model III in which both cerium ions at the edge were replaced by dopants.

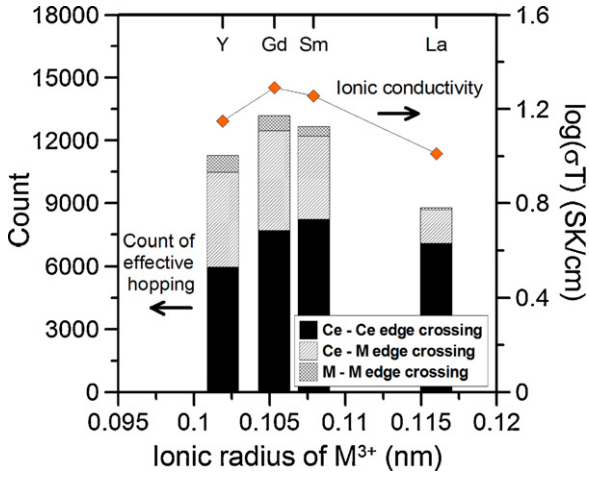

Fig. 9. Count of effective hopping recorded in $Ce_{0.8}M_{0.2}O_{1.9}$ during a 5 ns simulation, run at 1073 K. The simulated ionic conductivity ($\log(\sigma T)$) is also shown for comparison.

From the images of the NEB calculations and MD trajectories, the oxygen hopping path was found to be very close to a straight line. The 3rd image of the NEB calculations is related to the peak of energy profile with the hopping oxygen located at the midpoint of the two edge cations. From the atomic relaxation configurations of this image, we observed that the two edge cations slightly relaxed in an opposite direction toward ⟨1 1 0⟩ to enlarge the distance in-between. Taking Model III as an example, we found that the relaxation of larger-sized dopants on the edge was more apparent and the order of barrier height for different dopants before/after relaxation remained unchanged. This implies that the barrier height should mainly result from the fact that the larger dopant will yield a greater degree of electron cloud overlapping to discourage hopping.

We performed and analyzed oxygen hopping processes in details to assess the overall edge-blocking effect in MD simulation. By analyzing the trajectories of atoms, the oxygen (vacancy) hopping events were recorded. In order to correlate the count of hopping with ionic conductivity, we excluded the back-and-forth jumpings since they did not contribute to the overall displacement. The rest of jumping events were then defined as "effective hopping". The counts of effective hopping events for all the investigated ceria are shown in Fig. 9. We observed that the fraction of hops across Ce–M and M–M edges for the larger dopant cases (La and Sm) were significantly less than those for the smaller dopant size cases (Y and Gd). This finding was consistent with the energy barrier results shown in Table 2. The decrease of the counts of M–Ce and M–M edge-crossing became noticeable in the M = Sm case. This implies that the number of available hopping paths has been restricted as $r(M^{3+}) > r(Gd^{3+})$. Thus, the defect association analysis together with the edge-blocking effect gives a plausible interpretation for the best conductivity being found when M = Gd.

4. Conclusions

In the present work, the effect of four dopants (M^{3+}) on ionic conduction behavior of $Ce_{1-x}M_xO_{2-x/2}$ was studied. MD simu-

lations of Y-, Gd-, Sm- and La-doped ceria with $r(M^{3+})$ ranging from 1.019 to 1.160 Å were conducted. The calculated results of several important characteristics of ionic conductivity, e.g., $\log(\sigma T) - r(M^{3+})$ relationship and optimal dopant level, were in general agreement with experimental results. In contrast to the earlier simulation studies, which were performed under 0 K and low dopant concentration,[9–11] we modeled $Ce_{1-x}M_xO_{2-x/2}$ at various compositions and temperatures and investigated the atomistic mechanism of ionic conduction. The major observations from our calculations are summarized below:

1. From the analysis of vacancy trapping, oxygen vacancies in $Ce_{1-x}M_xO_{2-x/2}$ were found to be trapped at the first-neighbor of dopant cations for M = Y, Gd and Sm. However, the tendency of the second-neighbor trapping appeared to be more pronounced as $r(M^{3+})$ increased. For M = La, second-neighbor trapping of vacancies to M^{3+} was preferred over first-neighbor trapping.
2. For the cases where M = Y and La, the deep-trapping sites (with occupancy ≤ 0.5) trap more oxygen vacancies (23% and 34%, respectively) than those where M = Gd and Sm (∼10% for both). The trapping analysis supports our prediction that Gd and Sm dopants results in higher ionic conductivity than Y and La dopants.
3. It was found that even at high dopant levels, the vacancy-trapping mechanism still gives better interpretation to the overall order of ionic conductivity over the edge-blocking mechanism. However, the results that Gd–CeO_2 exhibits the highest conductivity can only be satisfactorily explained by consideration of the interplay of vacancy trapping and edge-blocking effects.

Acknowledgements

This research project was financially supported by National Science Council (project no. NSC96-2221-E-002-160-MY2). The authors would also like to acknowledge National Center for High-performance Computing and the Information Networking Center, National Taiwan University for providing high-performance computing facilities.

References

1. Steele BCH, Heinzel A. Materials for fuel-cell technologies. *Nature* 2001;**414**:345–52.
2. Inaba H, Tagawa H. Ceria-based solid electrolytes – review. *Solid State Ionics* 1996;**83**:1–16.
3. Kilner JA. Fast anion transport in solids. *Solid State Ionics* 1983;**8**:201–7.
4. Kim DJ. Lattice-parameters, ionic conductivities, and solubility limits in fluorite-structure MO_2 oxide ($M = Hf^{4+}$, Zr^{4+}, Ce^{4+}, Th^{4+}, U^{4+}) solid-solutions. *J Am Ceram Soc* 1989;**72**:1415–21.
5. Kilner JA. Defects and conductivity in ceria-based oxides. *Chem Lett* 2008;**37**:1012–5.
6. Butler V, Catlow CRA, Fender BEF, Harding JH. Dopant ion radius and ionic conductivity in cerium dioxide. *Solid State Ionics* 1983;**8**:109–13.
7. Minervini L, Zacate MO, Grimes RW. Defect cluster formation in M_2O_3–Doped CeO_2. *Solid State Ionics* 1999;**116**:339–49.
8. Wei X, Pan W, Cheng L, Li B. Atomistic calculation of association energy in doped ceria. *Solid State Ionics* 2009;**180**:13–7.
9. Andersson DA, Simak SI, Skorodumova NV, Abrikosov IA, Johansson B. Optimization of ionic conductivity in doped ceria. *Proc Natl Acad Sci USA* 2006;**103**:3518–21.
10. Nakayama M, Martin M. First-principles study on defect chemistry and migration of oxide ions in ceria doped with rare-earth cations. *Phys Chem Chem Phys* 2009;**11**:3241–9.
11. Yoshida H, Inagaki T, Miura K, Inaba M, Ogumi Z. Density functional theory calculation on the effect of local structure of doped ceria on ionic conductivity. *Solid State Ionics* 2003;**160**:109–16.
12. Kilner JA, Steele BCH. Mass transport in anion-deficient fluorite oxides. In: *Nonstoichiometric oxides*. New York: S.O.T. Academic Press; 1981. p. 233–269.
13. Krishnamurthy R, Srolovitz DJ, Kudin KN, Car R. Effects of lanthanide dopants on oxygen diffusion in yttria-stabilized zirconia. *J Am Ceram Soc* 2005;**88**:2143–51.
14. Krishnamurthy R, Yoon YG, Srolovitz DJ, Car R. Oxygen diffusion in yttria-stabilized zirconia: a new simulation model. *J Am Ceram Soc* 2004;**87**:1821–30.
15. Meyer M, Nicoloso N, Jaenisch V. Percolation model for the anomalous conductivity of fluorite-related oxides. *Phys Rev B* 1997;**56**:5961–6.
16. Cheng CH, Lee SF, Hong CW. Ionic dynamics of an intermediate-temperature yttria-doped-ceria electrolyte. *J Electrochem Soc* 2007;**154**:E158–63.
17. Hayashi H, Sagawa R, Inaba H, Kawamura K. Molecular dynamics calculations on ceria-based solid electrolytes with different radius dopants. *Solid State Ionics* 2000;**131**:281–90.
18. Inaba H, Sagawa R, Hayashi H, Kawamura K. Molecular dynamics simulation of gadolinia-doped ceria. *Solid State Ionics* 1999;**122**: 95–103.
19. Bevan DJM, Summerville E. Mixed rare earth oxides. In: Gschneidner KA, Eyring L, editors. *Handbook on the physics and chemistry of rare earths*, vol. 3. North-Holland, New York, NY, USA: Elsevier; 1988. p. 401.
20. Smith W, Forester TR. DL_POLY_2.0: a general-purpose parallel molecular dynamics simulation package. *J Mol Graph* 1996;**14**:136–41.
21. Hoover WG. Canonical dynamics: equilibrium phase-space distributions. *Phys Rev A* 1985;**31**:1695.
22. Nosé S. A unified formulation of the constant temperature molecular-dynamics methods. *J Chem Phys* 1984;**81**:511–9.
23. Kresse G, Hafner J. Ab initio molecular-dynamics for open-shell transition-metals. *Phys Rev B* 1993;**48**:13115–8.
24. Kresse G, Furthmuller J. Efficient iterative schemes for ab initio total-energy calculations using a plane-wave basis set. *Phys Rev B* 1996;**54**:11169–86.
25. Perdew JP, Burke K, Ernzerhof M. Generalized gradient approximation made simple. *Phys Rev Lett* 1996;**77**:3865–8.
26. Blochl PE. Projector augmented-wave method. *Phys Rev B* 1994;**50**:17953–79.
27. Kresse G, Joubert D. From ultrasoft pseudopotentials to the projector augmented-wave method. *Phys Rev B* 1999;**59**:1758–75.
28. Monkhorst HJ, Pack JD. Special points for brillouin-zone integrations. *Phys Rev B* 1976;**13**:5188–92.
29. Jonsson H, Mills G, Jacobsen KW. Nudged elastic band method for finding minimum energy paths of transitions. In: Berne B, Ciccotti G, Coker D, editors. *Classical and quantum dynamics in condensed phase simulations*. Singapore: World Scientific; 1998. p. 385.
30. Henkelman G, Uberuaga BP, Jonsson H. A climbing image nudged elastic band method for finding saddle points and minimum energy paths. *J Chem Phys* 2000;**113**:9901–4.
31. Gale JD. GULP: a computer program for the symmetry-adapted simulation of solids. *J Chem Soc, Faraday Trans* 1997;**93**:629–37.
32. Murch GE. The Nernst–Einstein equation in high-defect-content solids. *Philos Mag A-Phys Condens Matter Struct Defect Mech Prop* 1982;**45**:685–92.
33. Eguchi K, Setoguchi T, Inoue T, Arai H. Electrical-properties of ceria-based oxides and their application to solid oxide fuel-cells. *Solid State Ionics* 1992;**52**:165–72.
34. Balazs GB, Glass RS. Ac-impedance studies of rare-earth-oxide doped ceria. *Solid State Ionics* 1995;**76**:155–62.

35. VanHerle J, Horita T, Kawada T, Sakai N, Yokokawa H, Dokiya M. Low temperature fabrication of (Y,Gd,Sm)-doped ceria electrolyte. *Solid State Ionics* 1996;**86–88**:1255–8.
36. Mogensen M, Sammes NM, Tompsett GA. Physical, chemical and electrochemical properties of pure and doped ceria. *Solid State Ionics* 2000;**129**:63–94.
37. Zhang TS, Ma J, Kong LB, Chan SH, Kilner JA. Aging behavior and ionic conductivity of ceria-based ceramics: a comparative study. *Solid State Ionics* 2004;**170**:209–17.
38. Guan XF, Zhou HP, Liu ZH, Wang YA, Zhang J. High performance Gd^{3+} and Y^{3+} co-doped ceria-based electrolytes for intermediate temperature solid oxide fuel cells. *Mater Res Bull* 2008;**43**: 1046–54.
39. Steele BCH. Appraisal of $Ce_{1-y}Gd_yO_{2-y/2}$ electrolytes for IT-SOFC operation at 500 °C. *Solid State Ionics* 2000;**129**:95–110.
40. Zhan ZL, Wen TL, Tu HY, Lu ZY. Ac impedance investigation of samarium-doped ceria. *J Electrochem Soc* 2001;**148**:A427–32.
41. Faber J, Geoffroy C, Roux A, Sylvestre A, Abelard P. A systematic investigation of the dc-electrical conductivity of rare-earth doped ceria. *Appl Phys A: Mater Sci Process* 1989;**49**:225–32.
42. Suda E, Pacaud B, Mori M. Sintering characteristics, electrical conductivity and thermal properties of la-doped ceria powders. *J Alloy Compd* 2004;**408**:1161–4.
43. Chiang YM, Birnie DP, Kingery WD. *Physical Ceramics: Principles for Ceramic Science and Engineering*. Wiley, John & Sons, Incorporated; 1996.
44. Montgomery DC, Runger GC, Huble NF. *Engineering statistics*. Hoboken, NJ: John Wiley; 2007.
45. Navrotsky A, Simoncic P, Yokokawa H, Chen WQ, Lee T. Calorimetric measurements of energetics of defect interactions in fluorite oxides. *Faraday Discuss* 2007;**134**:171–80.
46. Pornprasertsuk R, Ramanarayanan P, Musgrave CB, Prinz FB. Predicting ionic conductivity of solid oxide fuel cell electrolyte from first principles. *J Appl Phys* 2005;**98**.